Joule

Article

Demonstrating black-diamond-based high-temperature solar cells

Graphical abstract

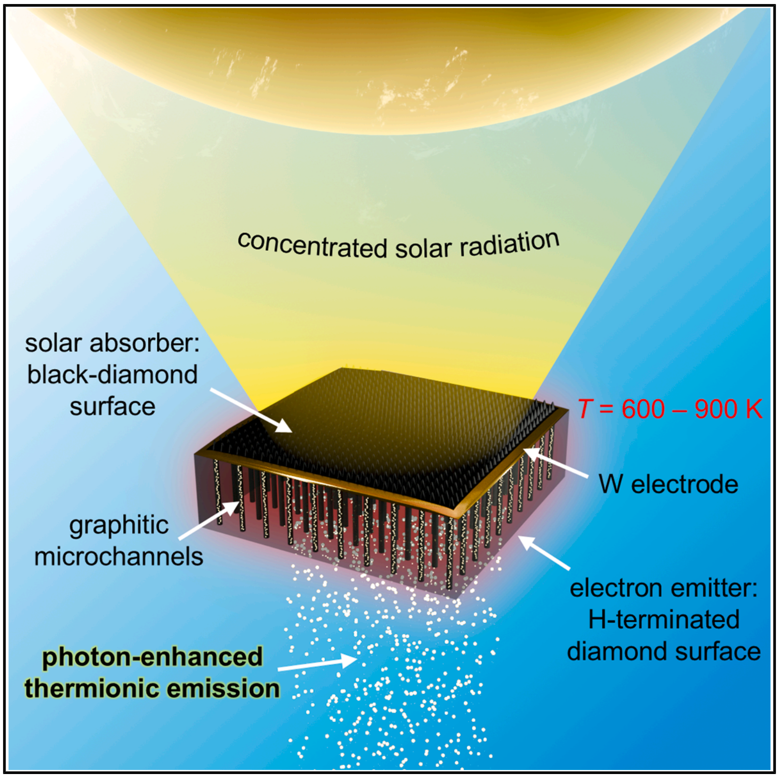

Highlights

- Black-diamond PETE cathode technology was discussed, developed, and tested
- Related converters demonstrated active power conversion under concentrated sunlight
- Cathode thickness was identified as the key parameter for maximizing efficiency
- Optimal cathodes could reach 30.3% QE and allow 14.5% solar conversion efficiency

Authors

Alessandro Bellucci, Marco Girolami, Matteo Mastellone, ..., Riccardo Polini, Abraham Kribus, Daniele M. Trucchi

Correspondence

danielemaria.trucchi@cnr.it

In brief

Black-diamond PETE cathodes enable scalable, concentrated solar energy conversion at high temperature. Optimized structures could achieve 14.5% solar-to-electric conversion and offer a cost-competitive, solid-state solution compatible with additional converters for enhanced overall efficiency and with thermal energy storage systems for flexible energy dispatch.

Bellucci et al., 2026, Joule *10*, 102223
January 21, 2026 © 2025 The Author(s). Published by Elsevier Inc.
https://doi.org/10.1016/j.joule.2025.102223

CellPress

Please cite this article in press as: Bellucci et al., Demonstrating black-diamond-based high-temperature solar cells, Joule (2025), https://doi.org/10.1016/j.joule.2025.102223

Joule

CellPress
OPEN ACCESS

Article

Demonstrating black-diamond-based high-temperature solar cells

Alessandro Bellucci,[1] Marco Girolami,[1] Matteo Mastellone,[2] Alessio Mezzi,[3] Valerio Serpente,[1] Stefano Orlando,[2] Antonio Santagata,[2] Riccardo Polini,[4] Abraham Kribus,[5] and Daniele M. Trucchi[1,6,*]

[1]ISM-CNR, Istituto di Struttura della Materia of the National Research Council (CNR), DiaTHEMA Lab, Montelibretti Unit, Via Salaria km 29.3, 00015 Monterotondo (Rome), Italy

[2]ISM-CNR, Istituto di Struttura della Materia of the National Research Council (CNR), FemtoLab, Tito Scalo Unit, Zona Industriale, 85050 Tito Scalo (PZ), Italy

[3]ISMN-CNR, Istituto per lo Studio dei Materiali Nanostrutturati of the National Research Council (CNR), Via Salaria km 29.3, 00015 Monterotondo (Rome), Italy

[4]Dipartimento di Scienze e Tecnologie Chimiche, Università di Roma “Tor Vergata”, Via della Ricerca Scientifica 1, 00133 Rome, Italy

[5]School of Mechanical Engineering, Tel Aviv University, Ramat Aviv, Tel Aviv 69978, Israel

[6]Lead contact

*Correspondence: danielemaria.trucchi@cnr.it

https://doi.org/10.1016/j.joule.2025.102223

CONTEXT & SCALE Concentrated solar power (CSP) represents an appealing solution for sustainable energy production, primarily due to its potential to reduce the levelized cost of produced energy compared to photovoltaic (PV) systems with battery storage. This advantage derives from the lower cost per surface area of sunlight collecting elements and compatibility with significantly cheaper thermal energy storage systems, favored by high-temperature operations. However, present CSP plants are economically competitive with PV-storage systems only at capacities larger than 100 MW. This limitation arises from the intrinsic difficulty in downscaling thermomechanical engines and cycles used in CSP, the conversion efficiency and cost of which drastically depend on the size. In contrast, solid-state converters such as PV cells are fundamentally scalable. All the attempts to integrate PV cells to CSP, including highly efficient concentrated PV cells, have failed commercially, mainly due to incompatibility with thermal energy storage. Other solid-state converters operating with photons and heat could solve this issue.

In 2010, Schwede et al. introduced the concept of photon-enhanced thermionic emission (PETE) converters as a more efficient alternative to PV cells. PETE occurs from a semiconducting cathode, stimulated by both photocarriers’ generation and thermalized solar energy, toward a collecting anode. Thermalization and absorption phenomena are considered inefficiencies in PV; conversely, within a PETE cathode, they enhance energy conversion by increasing the cathode temperature under solar irradiation. This concept paves the way for high-temperature solid-state solar cells suitable for CSP, potentially overcoming long-standing scalability limitations while ensuring compatibility with thermal energy storage. Active cathodes based on III–V semiconductors were developed to demonstrate PETE mechanism. However, the cathodes faced unsolved issues, including reduced stability of the electron-emission coating. Moreover, a complete and robust converter still has to be released. This represents a compulsory challenge for a competitive application in scalable CSP systems.

SUMMARY

Efficient high-temperature solar cells are feasible through the photon-enhanced thermionic emission (PETE) mechanism. The development of defect-engineered black-diamond layers, combined with micro-graphitized electrodes fabricated within p-type/intrinsic structures, represents the key technology for sunlight interaction of 0.3-eV electron-affinity PETE diamond cathodes, characterized by excellent electron emission. The resulting PETE converters demonstrate energy generation under concentrated radiation. At operating temperatures ranging from 600 to 900 K, the PETE operational regime is revealed, whereas photoemission and thermionic emission are found to be predominant at lower and higher temperatures, respectively. Cathode thickness emerges as the primary factor limiting the present performance of black-diamond technology.

Joule 10, 102223, January 21, 2026

Please cite this article in press as: Bellucci et al., Demonstrating black-diamond-based high-temperature solar cells, Joule (2025), https://doi.org/10.1016/j.joule.2025.102223

The generation-recombination analytical model applied to the device allows predicting a quantum efficiency of 30.3% for a 300-nm-thick black-diamond cathode operating at 700 K, today attainable with advanced diamond membrane technologies, and a solar-to-electric conversion efficiency of 14.5% for the resulting PETE converter.

INTRODUCTION

Solid state converters like concentrated photovoltaic (CPV) cells have been applied to concentrated solar power (CSP) applications. Although CPV cells are characterized by a high conversion efficiency approaching 50% given by multi-junction structure,[1] their application to CSP experienced difficulties especially in operating at high temperature, since such conditions correspond to a significant CPV cell's efficiency reduction and consequent incompatibility with any kind of thermal energy storage.

The concept for photon-enhanced thermionic emission (PETE) devices was proposed as a more efficient solution than PV cells to exploit direct photogeneration in a semiconducting absorber, as well as sub-bandgap photon absorption and thermalized energy induced by over-bandgap photons, which are detrimental in PV cells.[2] The resulting PETE semiconducting cathodes can effectively utilize both photons and excess thermal energy generated under high solar flux conditions. A PETE converter has the same architecture of a thermionic energy converter (TEC). The hotter cathode is directly illuminated by the concentrated sunlight and emits electrons toward a cooler anode, generating power across an electronic load connecting the two electrodes.[3,4] In PETE cathodes, a temperature increase favors the thermal distribution of emitting electrons, thus increasing electron emission. Moreover, PETE converters provide thermal energy to the anode that can be exploited in CSP by secondary stages like energy storage systems or secondary conversion stages. The overall efficiency can overcome both Shockley-Queisser photovoltaic and Carnot thermodynamic limits. Analytical models predict that a PETE device with an optimal 1.4-eV bandgap absorber can achieve conversion efficiencies as high as 52% under a radiation flux of 100 W cm^{-2}, and even 63% if integrated with a secondary thermal cycle converter.[5] According to such analytical models, the efficiency tends to increase with concentration ratio. However, at high temperatures other loss mechanisms become predominant, such as thermal emittance and heat dissipation at the electrical connectors. The main advantage over TECs is that PETE cathodes can operate at far lower temperatures than pure thermionic cathodes (>1,000°C) with equal work-function, since the opening of quasi-Fermi levels in the semiconducting absorber, caused by photon absorption, reduces the energy barrier for the vacuum escape of electrons. This mechanism implies that the electron affinity, rather than the work-function, rules the electron emission mechanism.

Bandgap-engineered PETE cathodes based on III–V semiconductors were employed for the proper sunlight absorption and charge carrier generation.[2,6–9] According to the Shockley-Queisser limit,[10] an optimal solar absorber operating at room temperature (RT) with a 1.34 eV bandgap is desirable for maximizing the sunlight absorption. At higher operating temperatures, a bandgap reduction of 0.2–0.6 meV K^{-1} (Figure S1) has to be taken into account. However, the development of a thermally-stable emitter for an effective reduction of cathode electron affinity is highly challenging in III–V semiconductors.[6] Even more challenging is limiting the diffusion of one atomic species composing the active III–V semiconductor at high temperature, especially if it is a ternary or quaternary compound. Such a diffusion makes the semiconductor composition and related properties slowly changing during the expected long-time operations.

Among III–V semiconductors, GaN[2] and GaAs/AlGaAs[6] cathodes have been developed, achieving quantum efficiencies (QEs) of 0.14% under 330 nm wavelength laser and 1.4% under 850 nm laser, respectively. Improved Al_xGa_{1-x}/GaAs cathodes obtained QE values close to 5% at 90°C under 850 nm radiation.[7] However, only a few complete PETE converters have been reported in the literature. A notable experiment reported about 1% power conversion efficiency from a device consisting of a commercial GaAs photocathode and an AlGaAs/GaAs anode incorporating quantum wells, under illumination with discrete monochromatic radiation from 550 to 880 nm wavelength.[11] Another interesting proof-of-concept converter was based on a cathode consisting of carbon nanotube forests, able to efficiently trap impinging photons and trigger a localized light-induced heating.[12] PETE converters with graphene-based cathodes have been developed and fully tested under a 450-nm wavelength laser.[13] The scarcity of other released converters denotes the present challenges in advancing the PETE technology.

Wide bandgap semiconductors are generally highly stable in temperature. Among them, diamond is stable over 1500°C under vacuum condition and shows a high electron emission currents thanks to a low or even negative electron affinity (NEA) if surface terminated with hydrogen. Work-function values as low as 1.7 and 0.9 eV can be obtained by nitrogen[14] or phosphorous[15] doping, respectively. The hydrogen termination on diamond is stable up to about 780°C,[14] even though the 700°C temperature is effective for long time exposures (<100 h) in inducing hydrogen desorption and represents the temperature upper limit for efficient hydrogenated diamond cathodes. On the other hand, diamond has an indirect bandgap of 5.45 eV at RT, consequently it is transparent to visible light, which seemingly should exclude it from solar applications. Conversely, defect engineering applied to fabricate surface nanotextured black-diamond films represents the suitable solution. Black-diamond is a defect-engineered material in which electrically-active defects, acting as an intermediate band of defect levels,[16] are introduced by the interaction with ultrashort laser pulses.[17] Recently such an electrically-active defect band with about 1.8 eV energy has been found in black-diamond,[18] as well as an optical absorption center at about 1.3 eV, confined at the first diamond lattice layers and induced by sp^2-like defects.[19] It was demonstrated by our group that black-diamond can achieve high solar absorptance values and considerably enhanced photoelectrical sensitivity, which can increase of several orders of magnitude for sub-bandgap photons of wavelength up to 800 nm.[20]

Black-diamond-based PETE cathodes have been here developed, combined with suitable anodes and dielectric spacing technology, and tested under concentrated solar radiation under ultra-high vacuum conditions to demonstrate active energy operations and analyze the critical parameters governing their performance.

RESULTS AND DISCUSSION

The black-diamond cathode structure

Black-diamond surfaces developed in this work have been fabricated by fs-laser double-pulse technique with pulses delayed of 500 fs inducing a bidimensional pseudo-periodicity of 160 and 100 nm depth and achieving a solar absorptance of about 90%.[17] Solar absorptance of black-diamond with a deeper treated zone of 500 nm can be even as high as 99%,[21] however in that case the density of recombination centers in the resulting material was found to be too high for an efficient transport of photogenerated carriers. Black-diamond, acting as a solar absorber of the PETE cathode, can be combined to a 3D fs-laser-based micro-graphitization technology[22] and arranged into a p-type/intrinsic hydrogen-terminated structure in single-crystals to demonstrate for the first-time operability of the PETE-driven conversion mechanism, as shown in the structure scheme, band diagram, and picture in Figures 1A, 1B, and 1C, respectively. Specifically, the solar absorbing surface, where black-diamond technology is applied, has a p-type boron-doped layer (>10^{19} cm^{-3} nominal B concentration up to a depth of 150 nm from the surface corresponding to a resistivity ranging from 1.5 × 10^{2} Ω cm at RT down to 1.5 × 10^{-2} Ω cm at 350°C—see Figure S2C) with the function to separate photogenerated electrons from holes. The B-doped layer guarantees a low contact resistance layer for an ohmic junction with the frame-shaped molybdenum contact and contributes with additional sub-bandgap photon absorption induced by the defect levels, introduced by the doping process.[23] Boron in diamond has an extremely low diffusion coefficient,[24] estimated to be 5 × 10^{-22} cm^2 s^{-1} at 700°C, that ensures operational stability at the operating temperatures throughout the device lifetime. When the cathode is exposed, the equilibrium Fermi level splits into the quasi-Fermi levels for electrons $E_{F,n}$ and holes $E_{F,p}$, respectively. The holes are transported toward the external contact as depicted in the band diagram of Figure 1B, whereas the electrons promoted in the conduction band (CB) are injected within the intrinsic region, where their diffusion length L was reported to range from 150 to 250 μm in single crystal diamond.[25] The thickness of the intrinsic region should be far shorter than the electron diffusion length to maximize the electron transport to the emitting surface with enhanced emission probability enabled by the surface hydrogen termination. Here, three black-diamond PETE cathodes, differing only in the thickness d = 500 ± 25, 200 ± 10, and 100 ± 5 μm, respectively, have been designed and fabricated for the first time to demonstrate energy generation and to investigate the influence of electron diffusion transport toward the emitting surface on the device efficiency. In PETE energy converters the Fermi-Dirac distribution is upshifted to the quasi-Fermi level for electrons. Therefore the cathode electron affinity EA replaces the role of work-function Φ_K in TECs in governing the cathodic emission. The cathode emission current density J_K can be described by the modified Richardson-Dushman equation:[2]

$$\begin{aligned} J_K &= A_K T_K^2 e^{-\frac{\phi_K - \left(E_{F,n} - E_F\right)}{k_B T_K}} = qnv\, e^{-\frac{\mathrm{EA}}{k_B T_K}}, E_{F,n} \\ &= E_F + k_B T_K \ln\left(n / n_0\right), \end{aligned} \qquad \text{(Equation 1)}$$

where q is the electron charge, T_K the cathode temperature, k_B the Boltzmann constant, n the concentration of photogenerated electrons over the equilibrium concentration n_0, $v = \sqrt{(k_B T_K)/(2\pi m^*)}$ the mean velocity of electrons perpendicular to the emitting surface, with m^* the effective electron mass in the semiconducting cathode. Besides transporting photogenerated electrons to the emitting surface, where they can reflect until emission, the PETE cathode can operate in a mixed condition where thermal electrons following the standard Fermi-Dirac distribution are emitted. Since intrinsic diamond is highly resistive (>10^{13} Ω cm at RT, decreasing down to 10^{3} Ω cm at 700°C—see Figure S2A), a proper electron refilling to replace emitted electrons can be a bottleneck to achieve a steady-state thermionic current. The embedded 3D laser graphitization is then useful for developing conductive microchannels connecting the two surfaces, allowing for the transport of additional thermal electrons by diffusion mechanism toward the emitting surface. A 50 × 50 graphitic microchannel array (about 5 μm channel width, 150 μm inter-channel pitch) was found to be sufficiently conductive (0.49 Ω cm at RT, decreasing down to 0.37 Ω cm at 700°C—see Figure S2D)[26] to increase the pure thermionic emission by 5 orders of magnitude in a test cathode.[22] The emitting surface is hydrogen-terminated to ensure an efficient electron emission.

PETE converter and operating conditions

The PETE cathodes have been tested under a high-flux solar simulator in relevant conditions that mimic the converter's operations. Here the high-flux sunlight, reaching values up to 41.6 W cm^{-2} on the cathode absorbing area, produces charge carriers and contributes to heat the cathode with the excess energy (up to 760°C), resulting from all the thermalization mechanisms. Therefore, this is the first time that a complete PETE converter is effectively demonstrated in conditions comparable to the operating ones, differently from all the experiments reported up to now, where refined characterizations were performed only on the emission mechanisms of the cathode[12,27,28] or on a complete converter by separating the function of heating the device from its illumination, conducted with a low-power lamp or a monochromatic laser.[13,29,30]

The work-function of cathode emitting surface is mainly determined by the hydrogenated diamond, since the graphitic microchannels occupy only 0.14% of the active area. The Φ_K value was evaluated by dark thermionic emission measurements to be 3.25 ± 0.09 eV by best-fitting the related Richardson plot (Figure S3).

The anode is a BaF_x-coated single-crystal aluminum plate with a work-function measured to be 1.8 ± 0.1 eV at RT (Figure S4), which is water-cooled and reached the temperature of 90°C at

Please cite this article in press as: Bellucci et al., Demonstrating black-diamond-based high-temperature solar cells, Joule (2025), https://doi.org/10.1016/j.joule.2025.102223

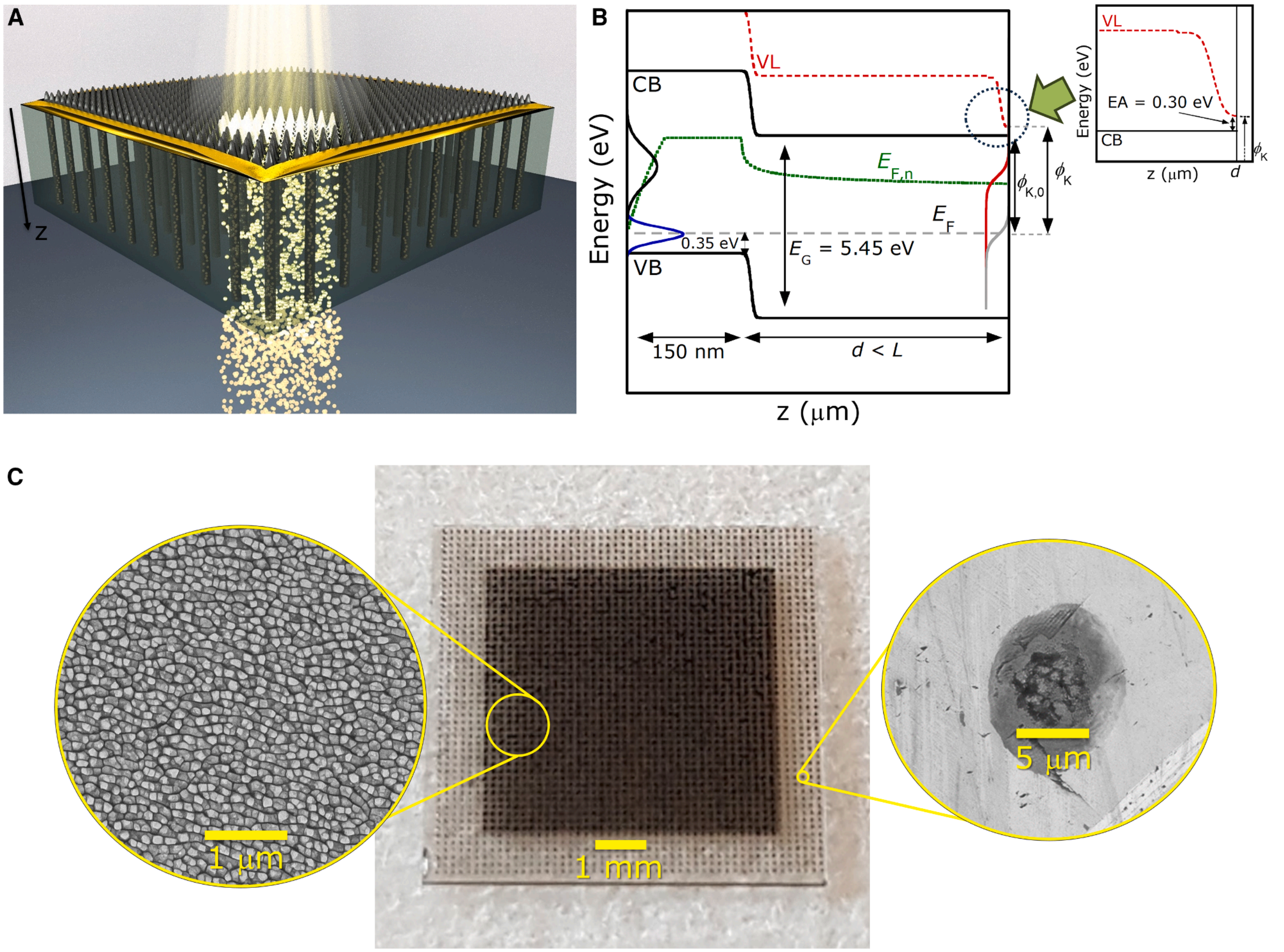

Figure 1. Schematic illustrations of PETE cathode operating mechanisms and picture of the assembled black-diamond cathode

(A) Pictorial sketch of the black-diamond PETE cathode under operation. The concentrated sunlight impinges on the nanotextured cathode surface, which absorbs the radiation and transforms photons into charge carriers. On such a surface an electric ohmic contact (gold color) is fabricated according to a frame geometry and, combined with a heavily p-type doped layer, allows for the collection of photogenerated holes and the recombination with thermal electrons injected by the external circuit. Conversely, photogenerated "hot" electrons (yellow circles) can diffuse within the diamond intrinsic bulk toward the emitting surface with high diffusion length *L*. At the same time, thermal electrons (dark red circles) can refill charge to the emitting surface through conductive graphitic microchannels. Then, both hot and thermal electrons with energy higher than the level of electron affinity EA, are emitted toward vacuum.

(B) Band diagram profile of the PETE cathode as a function of the PETE cathode depth z, where VB and CB are the valence and conduction band, respectively, and VL is the vacuum level. The black-diamond nanotexturing introduces a defect band within the bandgap at a given energy (black Gaussian curve), whereas B-doping introduces a narrower band around 0.35 eV over the VB (blue Gaussian curve), with the effect of downshifting the Fermi level E_F in the p-type layer. The promoted electrons in CB open the quasi-Fermi level $E_{F,n}$ and can travel toward the emitting surface thanks to diffusion mechanism, since the excess heat increases the device temperature and triggers the thermionic emission, thus resulting in a depleted region for electrons. If photoelectrons travel with a sufficient *L* with respect to the intrinsic region thickness *d*, they reach the emitting surface in the CB, where they find the EA barrier (found to be 0.3 eV and magnified in the inset). If electrons are reflected at the surface, they follow the non-equilibrium Fermi-Dirac statistics (red curve). At the same time, thermal electrons can be transported to the emitting surface through the graphitic microchannels at the equilibrium Fermi level and can be emitted according to the equilibrium Fermi-Dirac statistics (gray curve).

(C) Picture of an $8 \times 8 \times 0.2$ mm^3 black-diamond photocathode before metallization, where a 6×6 mm^2 black-diamond nanotexturing is performed on the central area of a previously B-ion implanted, thermally annealed, and selectively micro-graphitized diamond. Scanning electron micrographs show with detail the surface nanotexturing (left inset) and a graphitic microchannel (right inset).

the highest radiation power density (Figure S6B). The surface properties of BaF_x-coated anodes were found to be thermally stable in temperature up to at least 300°C, as revealed by a constant or even reduced work-function attributable to thermally-induced removal of surface oxides.[31] In the experiments, the vacuum inter-electrode gap was established to 100 ± 2 μm, that is a gap far higher than the ideal value (estimated between 0.9 and 3 μm,[32] and reduced to values ranging from 0.3 to 1 μm by more recent models).[33,34]

Converter's behavior under irradiation

The PETE cathode characterization was executed by alternating the dynamic recording of the emitted (and collected) current at an accelerating voltage of +5 V (electric field of 5×10^2 V

Please cite this article in press as: Bellucci et al., Demonstrating black-diamond-based high-temperature solar cells, Joule (2025), https://doi.org/10.1016/j.joule.2025.102223

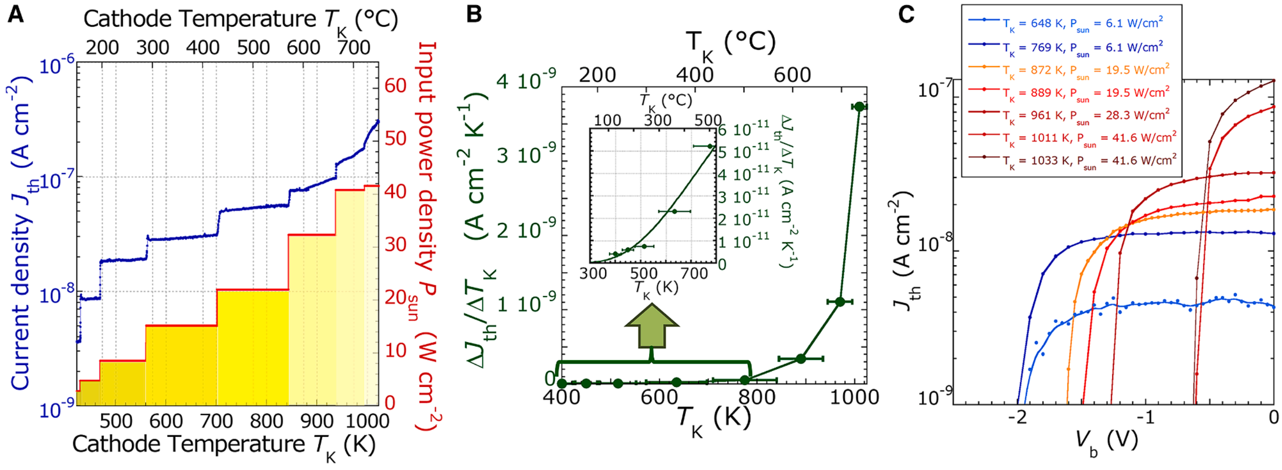

Figure 2. Analysis of device behavior under irradiation

(A) Emission current density J_{th} (blue dots) as a function of temperature while the cathode is illuminated by an increasing radiation power density (red lines) and a bias voltage of 5 V (corresponding to an accelerating electric field for electrons of 5×10^2 V cm^{-1}) is applied between the electrodes. It's worth observing that the temperatures achieved here by the cathode at a given input power density are lower than the temperature under steady-state conditions.

(B) Slope and related error bar of the $J_{th}(T_K)$ increments $\Delta J_{th}/\Delta T_K$, calculated by linearizing the current dependence on temperature. In the inset, the 400–800 K range is magnified to highlight the rapid increase of $\Delta J_{th}/\Delta T_K$ after $T_K > 600$ K, where the continuous curve represents the best-fit of the derivative of Equation 1 as a function of cathode temperature.

(C) Typical operating $J_{th}(V_b)$ characteristics provided by the converter with the thickest 500 μm cathode at different temperatures and radiation power densities in the retarding regime, demonstrating the active generation zone and the reduction of open-circuit and operating voltages as T_K approaches the highest values.

cm^{-1}, namely a value able to mitigate space charge effects due to the large inter-electrode gap) and steady state conditions for illumination and thermal conditions, where thermionic current density $J_{th}(V_b)$ characteristics were measured as a function of the voltage V_b applied between anode and cathode (a positive voltage corresponds to electron acceleration toward the anode). The cathode temperature is a variable depending on radiation power density (Figure S6A). Figure 2A shows the thermionic current measured dynamically as a function of the temperature at different illumination power densities. It can be observed that the emission current depends significantly on the radiation power density, thus demonstrating the effective optical and photoelectrical interaction of the black-diamond surface with the incoming solar radiation. The second observation refers to the dependence of the emission current density on the temperature at constant radiation flux: at temperatures approximately <600 K the current assumes an almost constant value depending predominantly on radiation power density, whereas for $T_K > 600$ K the current progressively shows a dependence on the growing temperature, that reveals the expected thermally-driven enhancement for the electron emission. It's worth observing that from 400 to 800 K, the slopes of $J_{th}(T_K)$ fit with high accuracy the expected derivative curve of Equation 1 as a function of temperature (Figure 2B), where the best-fit for EA returns the 0.30 ± 0.04 eV value. The emission current slope starts to assume significantly increasing values from $T_K > 600$ K, indicating the progressive emergence of a thermally-driven mechanism. Typical $J_{th}(V_b)$ characteristics, provided by the 500 μm-thick cathode under steady-state conditions, are shown in Figure 2C. The positive current under decelerating negative voltage demonstrates the net power generation of the PETE converter.

Figures 3A and 3B show the short-circuit current emission J_{sc} dependence on temperature T_K and radiation power density P_{sun}, respectively. The effective electron affinity value of the diamond PETE cathodes, derived from the application of Equation 1 to the J_{sc} dependence on temperature, confirms for all the cathodes the low but positive value of 0.30 ± 0.03 eV. A common EA value is expected since the properties of the cathodes' surfaces are comparable. The literature reports that hydrogen-covered domains are characterized by EA = −1.27 eV, whereas clean diamond surface returns EA = +0.38 eV.[35] The slightly positive EA found for the diamond surface can be attributed to an additional surface photovoltage forming under illumination at the hydrogenated diamond surface, caused by active surface defect states, and inducing a band-bending from NEA condition which progressively increases the effective work-function with respect to dark conditions.[36] This hypothesis is in agreement with the results discussed in the following. The emission current dependence on P_{sun} follows a power law close to linearity, with an exponent equal to 1.00 ± 0.10 for all the cathodes in the P_{sun} range from 4 to 20 W cm^{-2}.

Figure 3C shows the specific trend of the operating voltage V_{op} (i.e., the voltage maximizing the output power) as a function of temperature for the three cathodes, derived from the $J_{th}(V_b)$ characteristics. V_{op} increases with temperature up to $T_K = 600$ K, due to the progressive band-bending operated by filling of surface defect states and corresponding to the formation of an additional surface photovoltage.[36] This evidence is confirmed by the logarithmic trend for radiation power density $P_{sun} < 4$ W cm^{-2}, shown in Figure 3D, which is coherent with the progressive formation of a surface photovoltage under illumination. The increase of V_{op} from low input power density to the maximum values is limited to 0.30 ± 0.05 V for each different

Please cite this article in press as: Bellucci et al., Demonstrating black-diamond-based high-temperature solar cells, Joule (2025), https://doi.org/10.1016/j.joule.2025.102223

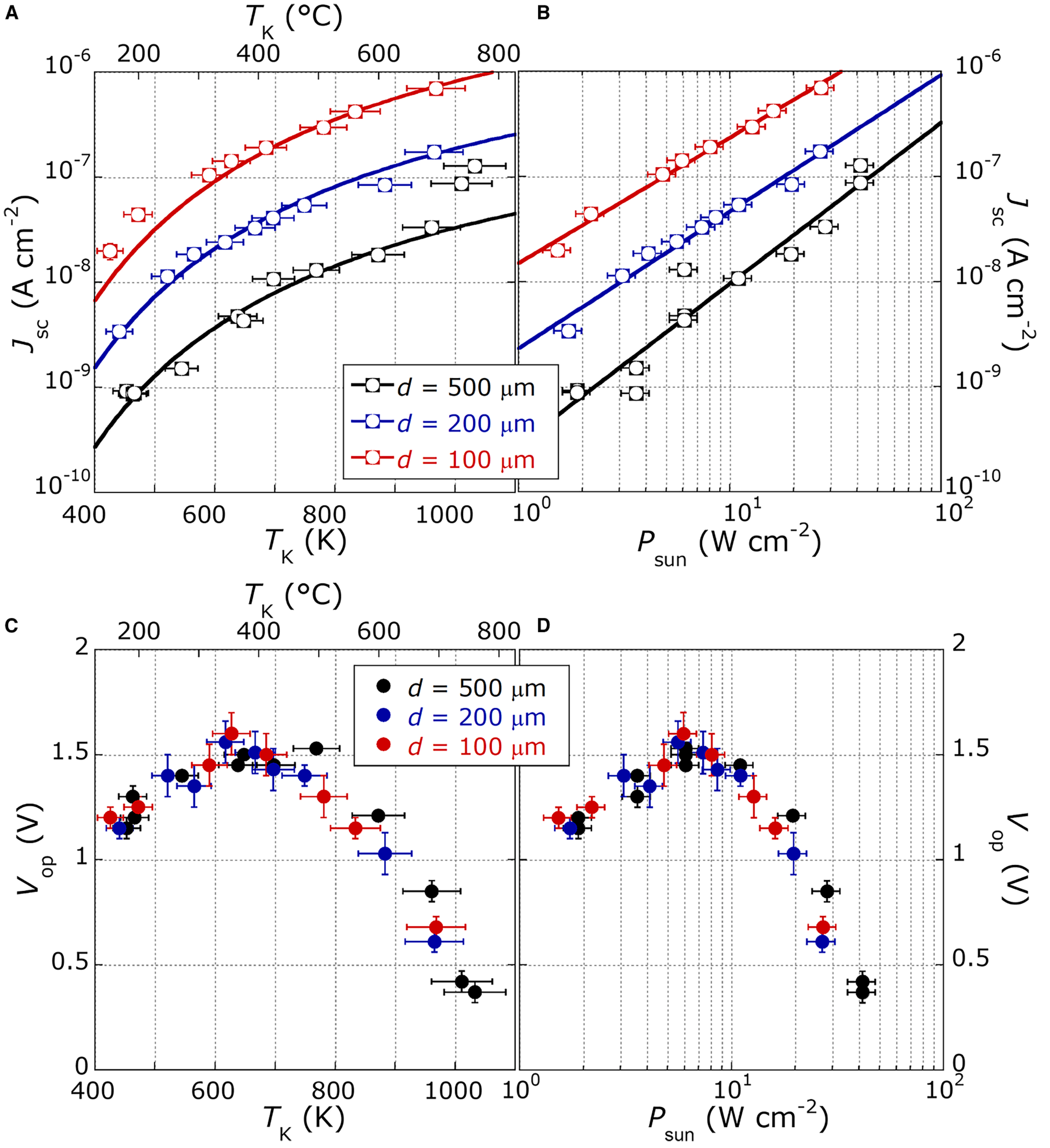

Figure 3. Output current density and operating voltage

Thermionic short-circuit current J_{sc} of converters based on different thickness black-diamond cathodes is reported as a function of (A) the cathode temperature T_K (solid lines represent the best-fit of Equation 1) and (B) the solar radiation power density P_{sun} (solid lines represent power-law best-fits). Operating voltages V_{op} provided by devices are shown as a function of (C) T_K and (D) P_{sun} show a maximum approximately in the 500–800 K range and for 5–12 W cm^{-2} input power density, respectively. The reduction of operating voltage values at the highest temperatures are in agreement with the $J_{th}(V_b)$ characteristics. Error bars visually quantify the related error.

Please cite this article in press as: Bellucci et al., Demonstrating black-diamond-based high-temperature solar cells, Joule (2025), https://doi.org/10.1016/j.joule.2025.102223

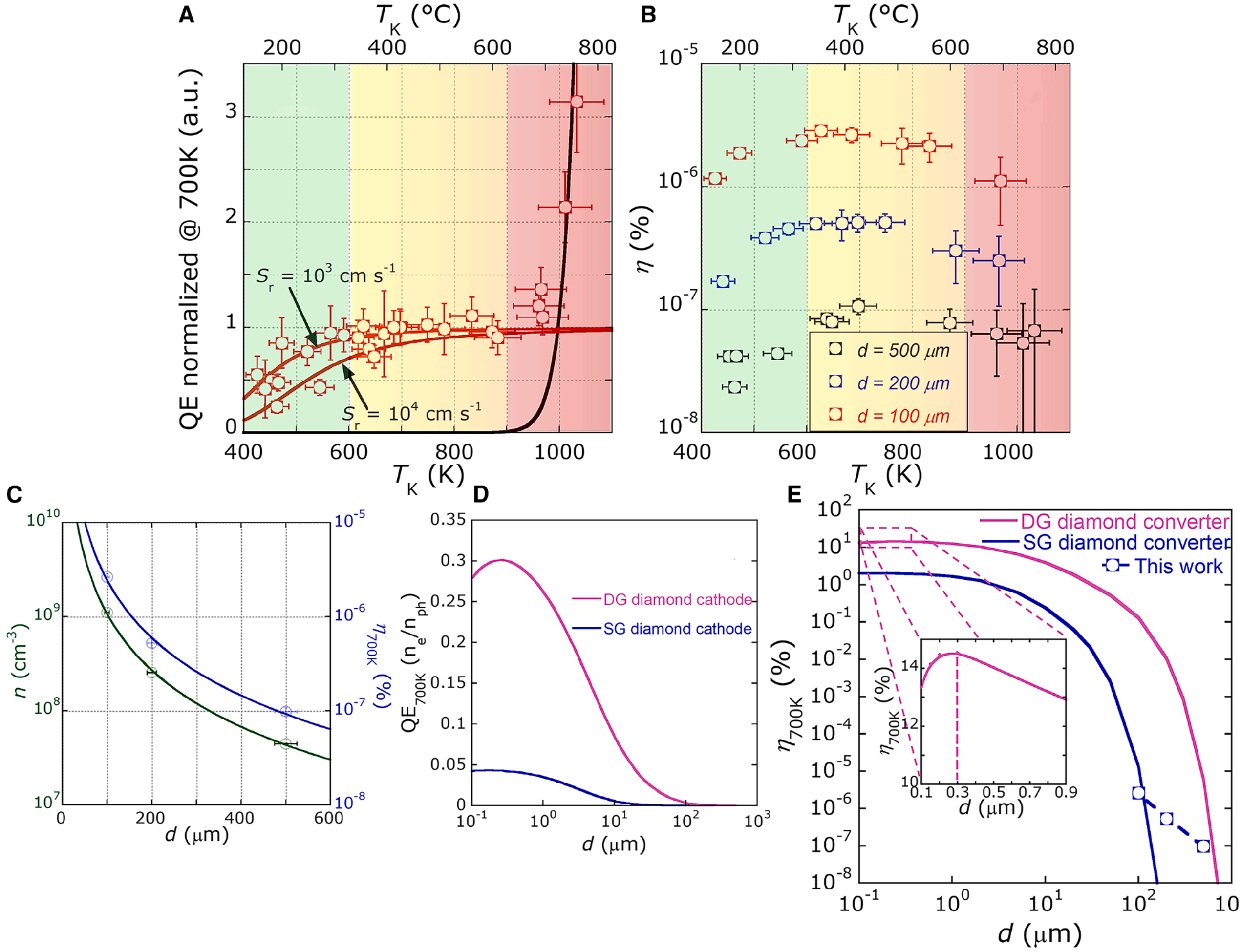

Figure 4. Evaluation of device performance as a function of critical parameters

(A) Normalized external quantum efficiency QE of all the devices as a function of T_K. Three regions can be clearly distinguished: direct photoemission ($T_K < 600$ K), PETE ($600 < T_K < 900$ K), and thermionic emission ($T_K > 900$ K) regime. Error bars visually quantify the related error. The two red curves represent the expected QE from the analytical model for a bulk cathode reported by Sahasrabuddhe et al.[37] with surface recombination velocity S_r of 10^3 and 10^4 cm s^{-1}, whereas the black curve depicts a Richardson-Dushman fit applied by using the measured effective work-function under illumination (3.55 eV).

(B) Solar-to-electric conversion efficiency η as a function of cathode temperature T_K, provided by the converters with different cathode thickness. It is evident that η is maximized between $600 \leq T_K \leq 800$ K.

(C) The excess electron concentration n, calculated as a fit parameter from Equation 1, and conversion efficiency at 700 K η_{700K} as a function of the cathode thickness d follow an inverse quadratic power law with exponent equal to -1.99 ± 0.04.

(D) The application of the analytical model reported by Sahasrabuddhe et al.[37] allows to derive QE$_{700K}$ as a function of d, for a detector grade (DG) and a standard-grade (SG) black-diamond cathode.

(E) Logarithmic plot of conversion efficiency upper limit as a function of d, indicating maximum values of 14.5% and 2.1% for a 300 nm detector-grade-based converter (magnified in a linear plot in the inset for visual aid) and a 200 nm standard-grade-based converter, respectively. The experimental data obtained in this work are indicated by the dashed line.

cathode, that is a value coherent with the EA derived from the analysis of current. The maximum V_{op} values are close to 1.6 V, that is actually larger than the expected difference between the "dark" cathode and anode work-functions. This finding strengthens the hypothesis that the effective cathode work-function under illumination increases with respect to the dark conditions $\Phi_{K,0}$, reaching the value $\Phi_K = \Phi_{K,0}$ + EA = 3.55 ± 0.14 eV. Between $600 < T_K < 800$ K, V_{op} is approximately constant. Finally, for temperatures higher than 800 K induced by radiation fluxes > 10 W cm^{-2}, a reduction in V_{op} occurs, which becomes steeper for $T_K > 900$ K, presumably due to the progressive shift of the emission mechanism from a photon-enhanced to a pure thermionic one.

Efficiency evaluation

Figure 4A shows the devices' normalized quantum efficiency QE as a function of T_K, namely the number of photogenerated, emitted, and collected electrons by the anode, per impinging photon able to promote them in the cathode CB. QE values were normalized at $T_K = 700$ K, where the conversion efficiency seems to achieve the maximum values for each cathode (Figure 4B). As can be observed, the resulting normalized QEs of the three cathodes almost superimpose, implying a similar behavior and allowing for the derivation of important parameters from the application of analytical models, with enhanced statistical significance. It's worth noting that QE is an increasing function of temperature until T_K reaches about 600 K and it is governed by the photoemission mechanism. Between 600 and 900 K, QE is approximatively constant, coherently with the expected PETE behavior. Finally, for $T_K > 900$ K, QE increases rapidly approaching the behavior of a thermionic energy converter, where additional electrons are merely thermally emitted. It must be stressed that the measured QE values are in excellent agreement with the behavior in temperature predicted by Schwede et al.,[2] and by the analytical model of Sahasrabuddhe et al.[37] up to 900 K (see supplemental information for details), whereas the QE data for $T_K > 900$ K are well fitted by the classic Richardson-Dushman equation of an emitter with work-function of 3.55 eV. The recombination velocity S_r on the emitting surface is an important fitting parameter that can be derived by applying the aforesaid analytical model. S_r is estimated to assume a value in the range 10^3–10^4 cm s^{-1} for the developed cathodes.

The conversion efficiency η of devices is defined as P_{out}/P_{sun}, where $P_{out} = J_{op} V_{op}$, namely the product of the output current density and voltage, respectively, at the maximum operating point. Figure 4B shows the temperature behavior of η, which reaches maximum values in the PETE regime between 600 and 800 K, where QE is maximum and thermal losses are moderate, especially if compared to the thermionic emission region at the highest temperatures. The conversion efficiency increases significantly with decreasing cathode thickness and reveals the critical role of d. The maximum conversion efficiency of 3×10^{-6}% provided by the 100 μm-thick cathode is low but comparable to a few other values reported in literature, such as 5×10^{-7}% and 2×10^{-5} % for devices consisting of cathodes made of graphene powder and aerogel, respectively,[13] even though these values were achieved under laser irradiation. A careful analysis is required to identify and understand the present bottlenecks in PETE technology. By applying Equation 1 to $J_{sc}(T_K)$ it is possible to derive n as a function of the cathode thickness d. It emerges clearly from Figure 4C that the lower the distance from photogeneration depth to the emitting surface, the higher the number of emitted electrons thanks to a reduced recombination, and the higher the conversion efficiency (see also Figure S7 reporting the quasi Fermi level opening relative to the equilibrium Fermi level position). Such an effect induces the same quadratic power law dependence as $n(d)$ and $\eta_{700K}(d)$, with exponent equal to -1.99 ± 0.04.

It's worth extrapolating what happens in conditions of thin-film cathodes' application, that is a realistically achievable technology by applying recent emerging procedures for fabrication of diamond membranes with thickness even down to 10 nm.[38] Particularly interesting is the exfoliation process of diamond films from the substrate to obtain large-area ultrathin and ultraflexible membranes,[39] for which the future application of the black-diamond PETE cathode processing seems to imply no technical limitations. Reported membrane technologies are connected with excellent surface and bulk physical properties of the resulting material, which have obviously an important role in enhancing the cathode QE. Indeed, if one considers the use of higher-quality diamond material than that used in this work, S_r can be indeed further reduced to values in the range 10^2–10^3 cm s^{-1} by using a detector-grade diamond,[40] thanks to a flatter surface (~0.5 vs. ~5 nm) and to a lower defect density (nominally from 2 to 3 orders of magnitude of N and B concentration). The lower defect density also causes an increase in the bulk diffusion coefficient (~50 vs. ~10 cm^2 s^{-1}).[41,42] Figure 4D shows QE at $T_K = 700$ K (where efficiency assumes maximum values) predicted for standard- and detector-grade diamond films as a function of d (details of the model for transmission-mode cathodes are described in the supplemental information). Both the curves increase of orders of magnitude as thickness reduces, indicating maximum values of $QE_{700K} = 0.30$ and $= 0.04$ for a 300 nm-thick detector-grade and a 200 nm-thick standard-grade cathode, respectively. It emerges also that the inverse quadratic power law of $n(d)$ and $\eta(d)$ represents a local approximation around $d = 100$ and 500 μm of the more complex exponential QE(d) dependence.

Interestingly, by deriving the expected upper-limit conversion efficiency at 700 K of the converters with standard-grade diamond cathodes, a very good matching at $d = 100$ μm emerges for experimental and predicted values. For thicker cathodes, the analytical values reveal a higher experimentally measured performance, suggesting that some parameters in the used materials could be actually higher than estimated (Figure 4E). Such an observation allows also determining that the vacuum transfer of electrons between the electrodes experiences negligible recombination. Anyway, the maximum conversion efficiency of a 300 nm detector-grade-based converter and a 200 nm standard-grade-based converter can be as high as 14.5% and 2.1%, respectively, which represents a significant starting point for a promising technology development, especially by observing that the device can be coupled with a secondary converter (e.g., thermoelectric generator, thermodynamic cycle or thermal energy storage system) operating on the residual heat on the PETE anode.

Conclusions

Single-crystal black-diamond PETE cathodes can be considered the archetype of defect-engineering applied to a wide bandgap semiconductor. Extension to thin diamond membranes, which can guarantee recombination and emission properties approaching the best single-crystal diamond material, seems to be feasible and represents the immediate technological perspective for the application to micro, linear, and point-focus concentrating systems, including solar towers, in terms of lower production costs, larger active areas, and higher efficiency. Black-diamond cathodes here reported have surprisingly and effectively interacted with concentrated sunlight. Anyway, the extension of such a defect-engineering to semiconductors with narrower bandgap than diamond, such as SiC,[17] can be an alternative medium-term technological challenge to provide future higher cost-effectiveness solutions for solar energy conversion. In addition to terrestrial applications, the resulting converters can be an effective solution for space exploration in extreme environments (high thermal gradients, permanently shadowed regions, etc.), acting as compact power-supplies for small robotics fed by intense laser beaming.[43]

METHODS

Fabrication of PETE cathodes

The black-diamond PETE cathodes developed in this work derive from the same single-crystal diamond plate with 8.0 × 8.0 × 1.2 mm^3 initial size ([B] < 0.05 ppm, [N] < 1 ppm), which has successively been cut into three plates (with thickness of 100 ± 5, 200 ± 10, and 500 ± 25 μm) and double-side polished (surface roughness of 5 nm). The diamond plate was preliminarily characterized in the dark as a function of temperature to derive electrical resistivity of the material, and it was irradiated by an X-ray beam, to derive the mobility-lifetime $\mu\tau$ product of the photocarriers. Figure S2A shows a typical behavior of resistivity, in which different activation energies can be clearly determined: $E_{A1} = 0.35 \pm 0.01$ eV, that can be attributed to the native boron (B) contamination owing to the typical B acceptor level in diamond; $E_{A2} = 1.20 \pm 0.03$ eV, that can be attributed to electrically-active defects; $E_{A3} = 1.95 \pm 0.02$ eV, which is a deep-level defect band. The application of the modified Hecht's equation to the photocurrent dependence on electric field allows us to evaluate the mean mobility-lifetime $\mu\tau$ product of the photocarriers $\mu\tau = 1.7 \times 10^{-4}$ cm^2 V^{-1} (Figure S2B). The mean mobility is therefore about 1.9×10^3 cm^2 V^{-1} s^{-1}, and the resulting mean carrier lifetime τ is about 90 ns.

The optimized technological steps for the fabrication of black-diamond PETE cathodes are:

Implantation and annealing of B ions on front surface to obtain a p-type layer

B ion implantation for p-type doping was performed at 40 keV implantation energy and a dose of 2×10^{15} ions cm^{-2}.[23] The samples were then rapid thermal annealed for 1 h at 1400°C under ultra-high-vacuum (UHV) conditions ($<10^{-8}$ mbar). The resulting sheet resistance was found to reduce from 10^{13} down to 10^7–10^8 Ω/square at RT after the annealing, corresponding to a p-type layer mean conductivity of about $1.5 \times (10^2$–$10^3)$ Ω cm at RT and an activation energy of 0.35 ± 0.01 eV (Figure S2C).

Fabrication of distributed microelectrodes by fs-laser graphitization

An array of 50 × 50 columns with a 150 μm inter-column pitch and 5 μm single-column diameter has been fabricated by a Spectra Physics Ti:sapphire femtosecond laser system coupled with a Newport μFAB workstation according to the following set of optimized parameters: 800 nm laser wavelength, 100 fs pulse duration, 1 kHz pulse repetition rate, 40× magnification objective lens with numerical aperture NA = 0.65, 7 μJ pulse energy, 64 μm s^{-1} vertical translation velocity. The cathodes were successively thermally annealed at 750°C under UHV conditions ($<10^{-8}$ mbar). The resistivity indicates two activation energies of 4.7 ± 0.6 and 26.1 ± 2.4 meV at the lower and higher temperatures, respectively (Figure S2D).

Fabrication of black-diamond surface

Nanoscale texturing on diamond plates' absorber surface (6 × 6 mm^2 area) was performed by a Spectra Physics Ti:sapphire femtosecond laser system coupled with a Michelson-like interferometer and a Newport μFAB workstation. A polarizing beam splitter generates two pulses from each ultrashort pulse, which have different optical paths and can be delayed and linearly polarized one perpendicularly to the other. The following set of optimized parameters were applied to treat the diamond plates in air: 800 nm laser wavelength, 100 fs pulse duration, 500 fs pulse delay, 1 kHz pulse repetition rate, 4× magnification objective lens with NA = 0.10 resulting in an ablation spot-size of 30 μm on the diamond surface, and 0.65 kJ cm^{-2} accumulated fluence. The resulting nanotexturing approximates a pseudo-2D periodic grating with a 160 nm periodicity and 100 nm height achieving a solar absorptance of about 90%,[17] evaluated by a spectrophotometer equipped with a 150 mm diameter Spectralon-coated integration sphere operating in the 0.3–2.5 μm wavelength range. A simple optical model aimed at disentangling the black diamond absorption from the underlying diamond plate one, treated as two distinct layers, allowed us to estimate an almost constant absorption coefficient of 1.3×10^5 cm^{-1} for the black-diamond over the explored wavelength.

Hydrogen-termination of emitting surface

Hydrogen termination was obtained by exposing the diamond plates to a hydrogen plasma produced by an Astex S1500 microwave-CVD system by using the following operating parameters: 300 standard cubic centimeter per minute (sccm), pre-vacuum pressure $< 10^{-7}$ mbar, 40 mbar process pressure, 700°C substrate temperature, 1.5 kW microwave power, 30 min process duration. The work-function was inferred to be 3.25 ± 0.09 eV by thermionic emission measurements in the dark (Figure S3).

Deposition of electric contacts

Tungsten contacts were deposited by DC magnetron sputtering from a 99.95% pure W target with 1-mm-width frame-shape, to surround the black diamond zone. The process parameters were: pre-vacuum pressure $< 5 \times 10^{-7}$ mbar, 2×10^{-2} mbar process argon pressure, substrate at RT. The cathodes were successively annealed at 650°C under UHV conditions ($<10^{-8}$ mbar) to thermally stabilize the contact and to avoid hydrogen desorption from the emitting surface. The consequent cathode sunlight-absorption area and electron-emission area are considered to be 6 × 6 mm^2 and 8 × 8 mm^2, respectively.

Development of the anode

The anode is made of a single-crystal aluminum plate (10 mm diameter, 1.0 mm thickness, (100) orientation, purity 99.99% surface polished with roughness < 10 nm, covered by a barium fluoride ultra-thin film (2 nm nominal thickness, 70% surface coverage and deposited according to the optimal recipe described by Serpente et al.[44] on a GaAs substrate), resulting in a work-function of 1.8 ± 0.1 eV measured at RT (Figure S4B).

Inter-electrode gap

The thermionic electrodes were separated by a vacuum gap established by a 100 ± 2 μm-thick quartz spacer, specifically fs-laser-cut into a ring-shape (8.0 and 7.0 mm for the external and internal diameter, respectively, to minimize the contact area and with a lateral gap of 1.0 mm to allow for an effective degassing from the inter-electrode vacuum volume).

Solar simulator

The solar simulator used is an imaging furnace fed by a short-arc 1 kW power Xe lamp, situated in the upper focus of a vertically oriented ellipsoid reflector, that illuminates a vacuum chamber containing the device, placed around the second focus of the reflector. The solar furnace is described in detail by Guesdon et al.[45] The lamp used is an OSRAM model XBO 1000W/HSO, that emits a spectrum approximating the solar one. The device can be moved vertically around the lamp focus to control its spot-size and radiation power density. Additionally, the lamp power can be controlled from 350 to 1,000 W by a stabilized power supply to vary the radiation power. The radiation power density was calibrated by a 1 cm-diameter ITI HT-50 heat flowmeter, mounted within the vacuum chamber in the exact cathode position. The cathode and anode temperatures are measured by K-type thermocouples mounted as close as possible to the thermionic electrodes, whereas a lateral ZnSb window allows the optical monitoring of temperature with a FLIR E95 IR thermal camera and/or a pyrometer Land-Minolta Cyclops-153A (for $T > 550^\circ$C). A previous calibration of the temperature measurement system was made by placing a thermocouple in the exact cathode position, in order to increase the measurement accuracy and evaluate the difference with respect to the position of the thermocouple mounted during the experiments out of the center of the beam. The vacuum level was kept in the range of 10^{-7} mbar during the photo-thermionic emission experiments by slowly increasing the incident radiation power.

Further details, including the scheme of experimental setup (Figure S5), are available in the supplemental information.

RESOURCE AVAILABILITY

Lead contact

For further information, contact Daniele M. Trucchi (danielemaria.trucchi@cnr.it).

Materials availability

Devices generated in this study will be made available on request, but we may require a reasonable compensation and/or a completed materials transfer agreement if there is potential for commercial application.

Data and code availability

All data may be provided by the authors upon reasonable request.

ACKNOWLEDGMENTS

The authors would like to thank Ionvac Process Srl; its CEO, Mr. Aniello Vitulano; and Dr. Gianfranco Sabbatella for the extremely valuable technical support in designing and fabricating the vacuum test chamber. The authors thank also Mr. Antonello Ranieri of IC-CNR and Mr. Fabrizio Pallotta of ISM-CNR for the technical valuable support. The authors gratefully acknowledge TECHPRO "Thermionic Energy Conversion for High Power RadiatiOn" project no. 2022KXKR3S funded by the Italian Ministry of University and Research within the framework of the EU Programme Next Generation Europe. This work reflects only the authors' views and opinions; neither the Ministry for University and Research nor the EuropeanCommission can be considered responsible for them.

AUTHOR CONTRIBUTIONS

Conceptualization, D.M.T; data curation, A.B., M.M., and D.M.T.; formal analysis, A.B. and D.M.T.; funding acquisition, D.M.T., A.K., and R.P.; methodology, A.B. and D.M.T. for design of testing setup and A.B., A.K., and D.M.T. for device testing procedure and calibration; investigation, A.B. and D.M.T. for device assembly and testing; M.G. and M.M. for diamond graphitization; S.O., A.S., A.B., and D.M.T. for laser texturing; R.P. for microscopy analysis; and A.M. for spectroscopy analysis; project administration and supervision, D.M.T.; visualization, V.S. and D.M.T.; writing – original draft, D.M.T.; review and editing, all the authors.

DECLARATION OF INTERESTS

The authors declare no competing interests.

SUPPLEMENTAL INFORMATION

Supplemental information can be found online at https://doi.org/10.1016/j.joule.2025.102223.

Received: July 7, 2025
Revised: September 15, 2025
Accepted: October 30, 2025

REFERENCES

1. Geisz, J.F., France, R.M., Schulte, K.L., Steiner, M.A., Norman, A.G., Guthrey, H.L., Young, M.R., Song, T., and Moriarty, T. (2020). Six-junction III–V solar cells with 47.1% conversion efficiency under 143 Suns concentration. Nat. Energy *5*, 326–335. https://doi.org/10.1038/s41560-020-0598-5.
2. Schwede, J.W., Bargatin, I., Riley, D.C., Hardin, B.E., Rosenthal, S.J., Sun, Y., Schmitt, F., Pianetta, P., Howe, R.T., Shen, Z.X., et al. (2010). Photon-enhanced thermionic emission for solar concentrator systems. Nat. Mater. *9*, 762–767. https://doi.org/10.1038/nmat2814.
3. Rahman, E., and Nojeh, A. (2021). Semiconductor thermionics for next generation solar cells: photon enhanced or pure thermionic? Nat. Commun. *12*, 4622. https://doi.org/10.1038/s41467-021-24891-2.
4. Campbell, M.F., Celenza, T.J., Schmitt, F., Schwede, J.W., and Bargatin, I. (2021). Progress Toward High Power Output in Thermionic Energy Converters. Adv. Sci. (Weinh) *8*, 2003812. https://doi.org/10.1002/advs.202003812.
5. Segev, G., Rosenwaks, Y., and Kribus, A. (2015). Limit of efficiency for photon-enhanced thermionic emission vs. photovoltaic and thermal conversion. Sol. Energy Mater. Sol. Cells *140*, 464–476. https://doi.org/10.1016/j.solmat.2015.05.001.
6. Schwede, J.W., Sarmiento, T., Narasimhan, V.K., Rosenthal, S.J., Riley, D.C., Schmitt, F., Bargatin, I., Sahasrabuddhe, K., Howe, R.T., Harris, J.S., et al. (2013). Photon-enhanced thermionic emission from heterostructures with low interface recombination. Nat. Commun. *4*, 1576. https://doi.org/10.1038/ncomms2577.
7. Wang, K., Wang, G., Chang, B., Tran, H., and Fu, R. (2017). Temperature dependence of photoemission characteristics from $Al_xGa_{1-x}As$/GaAs photocathodes. Appl. Opt. *56*, 6015–6021. https://doi.org/10.1364/AO.56.006015.
8. Zhuravlev, A.G., and Alperovich, V.L. (2017). Temperature dependence of photon-enhanced thermionic emission from GaAs surface with nonequilibrium Cs overlayers. Appl. Surf. Sci. *395*, 3–8. https://doi.org/10.1016/j.apsusc.2016.05.057.
9. Zhuravlev, A.G., Romanov, A.S., and Alperovich, V.L. (2014). Photon-enhanced thermionic emission from p-GaAs with nonequilibrium Cs overlayers. Appl. Phys. Lett. *105*, 251602. https://doi.org/10.1063/1.4904986.
10. Rühle, S. (2016). Tabulated values of the Shockley–Queisser limit for single junction solar cells. Sol. Energy *130*, 139–147. https://doi.org/10.1016/j.solener.2016.02.015.
11. Tereshchenko, O.E., Golyashov, V.A., Rodionov, A.A., Chistokhin, I.B., Kislykh, N.V., Mironov, A.V., and Aksenov, V.V. (2017). Solar energy converters based on multi-junction photoemission solar cells. Sci. Rep. *7*, 16154. https://doi.org/10.1038/s41598-017-16455-6.
12. Vahdani Moghaddam, M.V., Yaghoobi, P., Sawatzky, G.A., and Nojeh, A. (2015). Photon-Impenetrable, Electron-Permeable: The Carbon Nanotube

Forest as a Medium for Multiphoton Thermal-Photoemission. ACS Nano *9*, 4064–4069. https://doi.org/10.1021/acsnano.5b00115.

13. Guo, S., Zhao, H., Xu, Y., Pei, X., Li, S., Fu, Y., He, H., and Shen, X. (2022). Preparation of graphene aerogel and application in photon-enhanced thermionic emission. RSC Adv. *12*, 11113–11118. https://doi.org/10.1039/d2ra01219g.
14. Trucchi, D.M., Bellucci, A., Girolami, M., Calvani, P., Cappelli, E., Orlando, S., Polini, R., Silvestroni, L., Sciti, D., and Kribus, A. (2018). Solar Thermionic-Thermoelectric Generator (ST^{2}G): Concept, Materials Engineering, and Prototype Demonstration. Adv. Energy Mater. *8*. https://doi.org/10.1002/aenm.201802310.
15. Koeck, F.A.M., Nemanich, R.J., Lazea, A., and Haenen, K. (2009). Thermionic electron emission from low work-function phosphorus doped diamond films. Diam. Relat. Mater. *18*, 789–791. https://doi.org/10.1016/j.diamond.2009.01.024.
16. Luque, A., Martì, A., and Stanley, C. (2012). Understanding intermediate-band solar cells. Nat. Photonics *6*, 146–152. https://doi.org/10.1038/nphoton.2012.1.
17. Mastellone, M., Bellucci, A., Girolami, M., Serpente, V., Polini, R., Orlando, S., Santagata, A., Sani, E., Hitzel, F., and Trucchi, D.M. (2021). Deep-Subwavelength 2D Periodic Surface Nanostructures on Diamond by Double-Pulse Femtosecond Laser Irradiation. Nano Lett. *21*, 4477–4483. https://doi.org/10.1021/acs.nanolett.1c01310.
18. Girolami, M., Bellucci, A., Mastellone, M., Orlando, S., Pettinato, S., Serpente, V., Salvatori, S., and Trucchi, D.M. (2025). Two-Photon Sub-Bandgap Photocurrent in Surface-Nanotextured Black Diamond Films for Solar Energy Conversion. ACS Photonics *12*, 5874–5883. https://doi.org/10.1021/acsphotonics.5c00722.
19. Bellucci, A., Chemin, A., Petit, T., Bolli, E., Valentini, V., Cotts, B.L., Salleo, A., Girolami, M., Orlando, S., and Trucchi, D.M. (2025). Origin of surface-induced visible light absorption of nanostructured diamond. MRS Bull. https://doi.org/10.1557/s43577-025-00971-2.
20. Calvani, P., Bellucci, A., Girolami, M., Orlando, S., Valentini, V., Polini, R., and Trucchi, D.M. (2016). Black diamond for solar energy conversion. Carbon *105*, 401–407. https://doi.org/10.1016/j.carbon.2016.04.017.
21. Girolami, M., Bellucci, A., Mastellone, M., Orlando, S., Valentini, V., Montereali, R.M., Vincenti, M.A., Polini, R., and Trucchi, D.M. (2018). Optical characterization of double-nanotextured black diamond films. Carbon *138*, 384–389. https://doi.org/10.1016/j.carbon.2018.07.055.
22. Girolami, M., Criante, L., Di Fonzo, F., Lo Turco, S., Mezzetti, A., Notargiacomo, A., Pea, M., Bellucci, A., Calvani, P., Valentini, V., et al. (2017). Graphite distributed electrodes for diamond-based photon-enhanced thermionic emission solar cells. Carbon *111*, 48–53. https://doi.org/10.1016/j.carbon.2016.09.061.
23. Bellucci, A., Girolami, M., Calvani, P., Michaelson, S., Hofmann, A., Carcelen, V., and Trucchi, D.M. (2016). Buried Boron Doped Layer for CVD Diamond Photo-Thermionic Cathodes. IEEE Trans. Nanotechnol. *15*, 862–866. https://doi.org/10.1109/TNANO.2016.2566674.
24. Sung, T., Popovici, G., Prelas, M.A., and Wilson, R.G. (1995). Boron Diffusion Coefficient in Diamond. MRS Proc. *416*, 467–470. https://doi.org/10.1557/PROC-416-467.
25. Ristein, J., Stein, W., and Ley, L. (1997). Defect Spectroscopy and Determination of the Electron Diffusion Length in Single Crystal Diamond by Total Photoelectron Yield spectroscopy. Phys. Rev. Lett. *78*, 1803–1806. https://doi.org/10.1103/PhysRevLett.78.1803.
26. Mastellone, M., Bellucci, A., Girolami, M., Serpente, V., Polini, R., Orlando, S., Valentini, V., Santagata, A., Paci, B., Generosi, A., et al. (2022). Temperature-dependent electrical and structural characterization of laser-induced graphitic microwires in CVD diamond. Diam. Relat. Mater. *128*. https://doi.org/10.1016/j.diamond.2022.109294.
27. Sun, T., Koeck, F.A.M., Zhu, C., and Nemanich, R.J. (2011). Combined visible light photo-emission and low temperature thermionic emission from nitrogen doped diamond films. Appl. Phys. Lett. *99*, 202101. https://doi.org/10.1063/1.3658638.
28. Massicotte, M., Schmidt, P., Vialla, F., Watanabe, K., Taniguchi, T., Tielrooij, K.J., and Koppens, F.H. (2016). Photo-thermionic effect in vertical graphene heterostructures. Nat. Commun. *7*, 12174. https://doi.org/10.1038/ncomms12174.
29. Qiu, H., Xu, H., and Xiao, G. (2023). Hybrid photon-enhanced thermionic emission and photovoltaic converter with concentrated solar power. Sol. Energy Mater. Sol. Cells *254*. https://doi.org/10.1016/j.solmat.2023.112279.
30. Luo, S., Liao, S., Wang, C., Fu, Y., He, H., and Shen, X. (2024). Photon-enhanced thermionic emission solar cells based on boron-doped graphene/carbon nanosphere composite aerogel photocathode material. Appl. Opt. *63*, 4473–4479. https://doi.org/10.1364/AO.522584.
31. Bolli, E., Mezzi, A., Kaciulis, S., Serpente, V., Bellucci, A., and Trucchi, D.M. (2023). Temperature dependence of the work function in barium fluoride ultra-thin films on semiconductors for hybrid thermionic converters studied by ultraviolet photoelectron spectroscopy. Surf. Interface Anal. *55*, 541–547. https://doi.org/10.1002/sia.7182.
32. Lee, J.-H., Bargatin, I., Melosh, N.A., and Howe, R.T. (2012). Optimal emitter-collector gap for thermionic energy converters. Appl. Phys. Lett. *100*, 173904. https://doi.org/10.1063/1.4707379.
33. Jensen, D., Taufiq Elahi, A.N.M., Ghashami, M., and Park, K. (2021). Submicrometer-Gap Thermionic Power Generation Based on Comprehensive Modeling of Charge and Thermal Transport. Phys. Rev. Appl. *15*. https://doi.org/10.1103/PhysRevApplied.15.024062.
34. Rahman, E., and Nojeh, A. (2020). Interplay between Near-Field Radiative Coupling and Space-Charge Effects in a Microgap Thermionic Energy Converter under Fixed Heat Input. Phys. Rev. Appl. *14*. https://doi.org/10.1103/PhysRevApplied.14.024082.
35. Cui, J.B., Ristein, J., and Ley, L. (1998). Electron Affinity of the Bare and Hydrogen Covered Single Crystal Diamond (111) Surface. Phys. Rev. Lett. *81*, 429–432. https://doi.org/10.1103/PhysRevLett.81.429.
36. Schindler, P., Riley, D.C., Bargatin, I., Sahasrabuddhe, K., Schwede, J.W., Sun, S., Pianetta, P., Shen, Z.X., Howe, R.T., and Melosh, N.A. (2019). Surface Photovoltage-Induced Ultralow Work Function Material for Thermionic Energy Converters. ACS Energy Lett. *4*, 2436–2443. https://doi.org/10.1021/acsenergylett.9b01214.
37. Sahasrabuddhe, K., Schwede, J.W., Bargatin, I., Jean, J., Howe, R.T., Shen, Z.-X., and Melosh, N.A. (2012). A model for emission yield from planar photocathodes based on photon-enhanced thermionic emission or negative-electron-affinity photoemission. J. Appl. Phys. *112*. https://doi.org/10.1063/1.4764106.
38. Guo, X., Xie, M., Addhya, A., Linder, A., Zvi, U., Wang, S., Yu, X., Deshmukh, T.D., Liu, Y., Hammock, I.N., et al. (2024). Direct-bonded diamond membranes for heterogeneous quantum and electronic technologies. Nat. Commun. *15*, 8788. https://doi.org/10.1038/s41467-024-53150-3.
39. Jing, J., Sun, F., Wang, Z., Ma, L., Luo, Y., Du, Z., Zhang, T., Wang, Y., Xu, F., Zhang, T., et al. (2024). Scalable production of ultraflat and ultraflexible diamond membrane. Nature *636*, 627–634. https://doi.org/10.1038/s41586-024-08218-x.
40. Grivickas, P., Ščajev, P., Kazuchits, N., Mazanik, A., Korolik, O., Voss, L.F., Conway, A.M., Hall, D.L., Bora, M., Subačius, L., et al. (2020). Carrier recombination parameters in diamond after surface boron implantation and annealing. J. Appl. Phys. *127*. https://doi.org/10.1063/5.0004881.
41. Grivickas, P., Ščajev, P., Kazuchits, N., Lastovskii, S., Voss, L.F., Conway, A.M., Mazanik, A., Korolik, O., Bikbajevas, V., and Grivickas, V. (2020). Carrier recombination and diffusion in high-purity diamond after electron irradiation and annealing. Appl. Phys. Lett. *117*. https://doi.org/10.1063/5.0028363.
42. Malinauskas, T., Jarašiūnas, K., Ivakin, E., Tranchant, N., and Nesladek, M. (2010). Determination of carrier diffusion coefficient and lifetime in single crystalline CVD diamonds by light-induced transient grating technique.

Physica Status Solidi (a) *207*, 2058–2063. https://doi.org/10.1002/pssa.201000100.

43. Algora, C., García, I., Delgado, M., Peña, R., Vázquez, C., Hinojosa, M., and Rey-Stolle, I. (2022). Beaming power: Photovoltaic laser power converters for power-by-light. Joule *6*, 340–368. https://doi.org/10.1016/j.joule.2021.11.014.
44. Serpente, V., Bellucci, A., Girolami, M., Mastellone, M., Mezzi, A., Kaciulis, S., Carducci, R., Polini, R., Valentini, V., and Trucchi, D.M. (2020). Ultra-thin films of barium fluoride with low work function for thermionic-thermophotovoltaic applications. Mater. Chem. Phys. *249*. https://doi.org/10.1016/j.matchemphys.2020.122989.
45. Guesdon, C., Alxneit, I., Tschudi, H.R., Wuillemin, D., Petrasch, J., Brunner, Y., Winkel, L., and Sturzenegger, M. (2006). PSI's 1kW imaging furnace—A tool for high-temperature chemical reactivity studies. Sol. Energy *80*, 1344–1348. https://doi.org/10.1016/j.solener.2005.04.028.